Clays and Clay Minerals, Vol. 61, No. 4, 375–391, 2013.

THICKNESS DISTRIBUTIONS AND EVOLUTION OF GROWTH MECHANISMS OF NH_4-ILLITE FROM THE FOSSIL HYDROTHERMAL SYSTEM OF HARGHITA BÃI, EASTERN CARPATHIANS, ROMANIA

IULIU BOBOS[1,*] AND D. D. EBERL[2]

[1] Centre of Geology, Faculty of Sciences, University of Porto, Portugal
[2] Emeritus Scientist, U.S. Geological Survey, 3215 Marine Street, Suite E127, Boulder, Colorado 80303-1066, USA

Abstract—The crystal growth of NH_4-illite (NH_4-I) from the hydrothermal system of Harghita Bãi (Eastern Carpathians) was deduced from the shapes of crystal thickness distributions (CTDs). The <2 μm and the <2−0.2 μm fractions of clay samples collected from the argillized andesite rocks consist of NH_4-illite-smectite (I-S) interstratified structures (R1, R2, and R3-type ordering) with a variable smectite-layer content. The NH_4-I-S (40−5% S) structures were identified underground in a hydrothermal breccia structure, whereas the K-I/NH_4-I mixtures were found at the deepest level sampled (−110 m). The percentage of smectite interlayers generally decreases with increasing depth in the deposit. This decrease in smectite content is related to the increase in degree of fracturing in the breccia structure and corresponds to a general increase in mean illite crystal thickness. In order to determine the thickness distributions of NH_4-I crystals (fundamental illite particles) which make up the NH_4-I-S interstratified structures and the NH_4-I/K-I mixtures, 27 samples were saturated with Li^+ and aqueous solutions of PVP-10 to remove swelling and then were analyzed by X-ray diffraction. The profiles for the mean crystallite thickness (T_{mean}) and crystallite thickness distribution (CTD) of NH_4-I crystallites were determined by the Bertaut-Warren-Averbach method using the *MudMaster* computer code. The T_{mean} of NH_4-I from NH_4-I-S samples ranges from 3.4 to 7.8 nm. The T_{mean} measured for the NH_4-I/K-I mixture phase ranges from 7.8 nm to 11.7 nm (NH_4-I) and from 12.1 to 24.7 nm (K-I).

The CTD shapes of NH_4-I fundamental particles are asymptotic and lognormal, whereas illites from NH_4-I/K-I mixtures have bimodal shapes related to the presence of two lognormal-like CTDs corresponding to NH_4-I and K-I.

The crystal-growth mechanism for NH_4-I samples was simulated using the *Galoper* code. Reaction pathways for NH_4-I crystal nucleation and growth could be determined for each sample by plotting their CTD parameters on an $\alpha-\beta^2$ diagram constructed using *Galoper*. This analysis shows that NH_4-I crystals underwent simultaneous nucleation and growth, followed by surface-controlled growth without simultaneous nucleation.

Key Words—Ammonium, Asymptotic Distribution, Crystal Thickness Distribution, Eastern Carpathians, Growth, Harghita Bãi Hydrothermal System, Illite, Lognormal Distribution, Nucleation, Surface-controlled Growth.

INTRODUCTION

Pioneering studies of the nucleation and growth of sphalerite (Verma, 1956; Komatsu and Sunagawa, 1965), biotite (Amelinck, 1952), hematite (Sunagawa, 1960, 1961, 1962), phlogopite (Sunagawa, 1964), calcite, and mica (Baronnet, 1982, 1984) called upon the spiral growth theory developed by Frank (1949) which predicts the presence of growth features in the form of very flat, spirally terraced hills on crystal faces that are perpendicular to a screw dislocation axis. A considerable amount of work dedicated to the nucleation and crystal-growth history of clay minerals in fossil and active hydrothermal systems has been done since the 1970s. Observations of kaolin-group minerals (Sunagawa and Koshino, 1975), pyrophyllites (Kitagawa, 1992), illites (Kitagawa, 1995), and mixed-layer I-S (Kitagawa and Matsuda, 1992) have shown the presence of spiral-shaped steps on the (001) faces of crystals formed from solutions with low supersaturation. Several authors, based on electron microscopy observations, advocated the mechanism of stepwise dissolution and crystallization of illite minerals (Nadeau *et al.*, 1985; Eberl *et al.*, 1987; Inoue *et al.*, 1988), or that of spiral growth on the (001) faces of illite (Blum, 1994) or on mixed-layer I-S (Kitagawa, 1995; Inoue and Kitagawa, 1994). Some of the results obtained have suggested Ostwald ripening as the growth mechanism (Eberl and Środoń, 1988; Inoue *et al.*, 1988), which proposes the simultaneous growth and dissolution of illite particles within a single medium. In contrast, Eberl *et al.* (1990) recognized that the illite samples analyzed did not express the CTD shape expected for the Ostwald ripening mechanism and, therefore, this mechanism is unlikely to have occurred.

* E-mail address of corresponding author:
ibobos@fc.up.pt
DOI: 10.1346/CCMN.2013.0610415

https://doi.org/10.1346/CCMN.2013.0610415 Published online by Cambridge University Press

The reaction history of clay minerals during diagenesis, hydrothermal activity, and low-grade metamorphism can be obtained by studying the evolution of the shapes of their crystallite-thickness distributions (Eberl *et al.*, 1998a; Środoń *et al.*, 2000; Bove *et al.*, 2002). Various laws generate distinctive crystal-distribution shapes during the geological history of crystal growth. In fact, different isotope ratios may be preserved in different I-S crystal-size fractions due to different mechanisms of crystal growth (Williams and Hervig, 2006). The CTD shapes are calculated from X-ray diffraction (XRD) data by applying the Bertaut-Warren-Averbach (BWA) method (Drits *et al.*, 1998), a method that gives both T_{mean} of illite crystallites parallel to c^* and the shapes of CTDs. These shapes were then simulated using the crystal-growth theory of Eberl *et al.* (1998a) and the computer program *Galoper* (Growth According to the Law of Proportionate Effect and Ripening; Eberl *et al.*, 2000). Such measurements of illite and smectite crystals using *MudMaster, Galoper*, and associated computer programs (Eberl, 2002; Eberl *et al.*, 1996, 2000) have been applied by several authors (Aldega and Eberl, 2005; Bove *et al.*, 2002; Brime and Eberl, 2002; Dudek *et al.*, 2002; Dudek and Środoń, 2003; Kotarba and Środoń, 2000; Mystkowski *et al.*, 2000; Warr and Nieto, 1998) in order to identify crystal-growth mechanisms and to follow the evolution of crystal thicknesses during reaction progress.

The aim of the present study was to describe the changes in NH_4-I crystallite thickness and crystal-growth evolution in NH_4-I-S mixed-layer clays, in NH_4-I/K-I mixtures, and to infer the early environment of NH_4-I crystallization from the shapes of their CTD. The evolution of the CTD shape of selected samples is followed using the *MudMaster* code, whereas their crystal-growth mechanism was simulated using the *Galoper* code.

GEOLOGICAL BACKGROUND

The Neogene volcanism of the Eastern Carpathians in the Carpathian orogen (Figure 1a) was related to subduction of the East European Plate beneath the Tisza–Dacia (Transylvanian) continental microplate (Rădulescu and Săndulescu, 1973; Săndulescu, 1984; Seghedi *et al.*, 1998, 2004), where its calc-alkaline materials range from dacitic to andesitic. The Călimani-Gurghiu-Harghita (CGH) area (Figure 1b) is the youngest volcanic unit of the Carpathians formed during an active island arc evolution (Bleahu *et al.*, 1973; Rădulescu *et al.*, 1973; Seghedi *et al.*, 1998, 2004). The CGH volcanic chain is viewed as an ideal volcanic structure, consisting of a central volcanic zone with an infrastructure of subvolcanic bodies and an intermediate zone corresponding to a volcanic cone and a peripheral volcanoclastic zone (Szakacs and Seghedi, 1995). The complex volcanic structure of Vârghis-Harghita Băi is located in the joins between craters of stratovolcanic compartments (Figure 1b). The absolute age of the andesitic rocks corresponding to the intermediate zone of the Vârghis-Harghita Băi volcanic structure ranges from 5.3 to 4.1 Ma (Upper Pliocene; Peltz *et al.*, 1987).

Porphyry-copper systems were recognized in several volcanic structures located in the axial part of the Gurghiu-Harghita mountains, being associated with Cu – Mo ± Au mineralization of Andean type (Stanciu, 1984). The hydrothermal area of Harghita Băi is the most important field of argillic alteration in the Neogene volcanic area of the Eastern Carpathians. The magmatic-hydrothermal fluids related to the evolution of the subvolcanic body (*i.e.* microdiorite or/and pyroxene andesite) have generated this geothermal field. A wide variety of calc-alkaline andesites (*e.g.* basaltic andesite, amphibole ± pyroxene ± biotite andesite) occur above the subvolcanic body. The alteration halo (biotite → amphibole → phyllic → argillic) associated with the porphyry copper system (Stanciu, 1984) is centered on the subvolcanic body of dioritic composition.

The hydrothermal area of Harghita Băi was investigated from the surface to a depth of 110 m, where propylitic, argillic, and advanced argillic alterations were identified (Bobos, 2000). Propylitic alteration identified at −110 m and −80 m corresponds to a di-smectite + epidote + calcite assemblage. A tri-smectite and chlorite/smectite-like corrensite assemblage was also identified in altered pyroxene andesitic rocks at −80 m. Several Al-clay assemblages well zoned from −80 m to the surface were identified, *e.g.* a sudoite + dickite assemblage, a Na-rectorite + K-illite assemblage, and well ordered kaolinite. Areas corresponding to advanced argillic alteration (Meyer and Hemley, 1967) characterized by kaolinite + pyrophyllite, kaolinite, dickite, and pyrophyllite assemblages occur from −50 to −30 m. Alunite, opal-C, boehmite, and zuniyte are associated either with kaolinite or pyrophyllite assemblages. Acid-sulfate zones also occur at the surface around the crater area.

The argillic alteration in the Harghita Băi corresponds to a high-sulfidation zone (Hedenquist and Lowenstern, 1994), essentially barren (*i.e.* free of metals), which makes a transition to a low-sulfidation zone with disseminated base metal and to the porphyry copper system recognized at depth (~1000 m) by previous authors (Stanciu, 1984).

A hydrothermal breccia pipe structure (BS) containing NH_4-I-S interstratified structures (40-5% S) was identified for the first time in the Harghita Băi area. Ammonium-illite was found in the barren part of the BS, where a conversion series of smectite to NH_4-I, as well as K-I/NH_4-I mixtures were described (Bobos and Ghergari, 1999; Bobos, 2012). The K-I/NH_4-I mixtures were found outside of the BS at −110 m in mine drifts.

The K-Ar dating of K-I/NH_4-I mixtures gave an age of 9.5 Ma, whereas the NH_4-I (sample HB-10) collected

https://doi.org/10.1346/CCMN.2013.0610415 Published online by Cambridge University Press

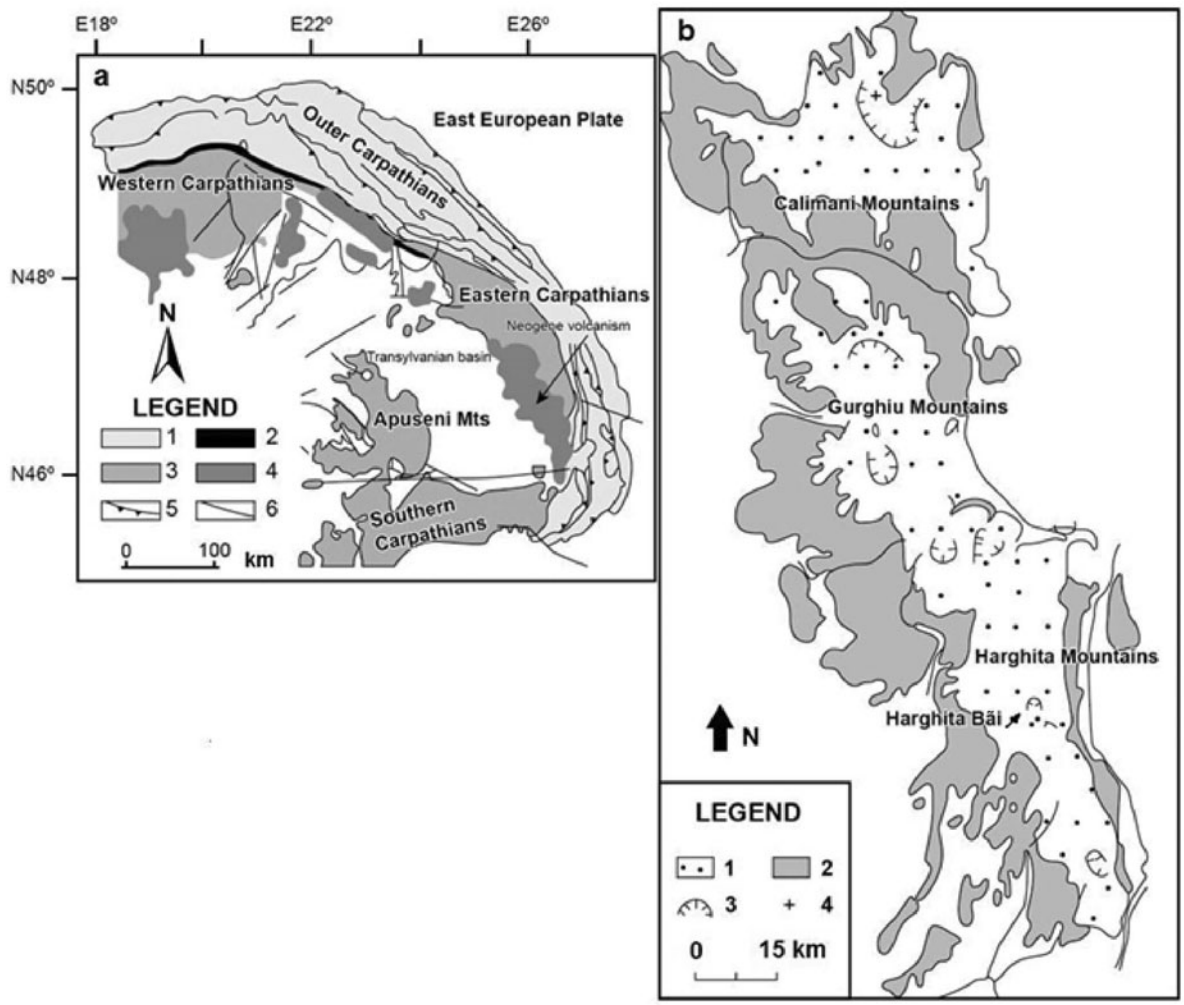

Figure 1. (a) Geotectonic sketch of the Carpatho-Pannonian area (adapted from Sãndulescu, 1984; Royden, 1988; Seghedi *et al.*, 1998, 2004) showing the major tectonic units and boundaries, and the main occurrence areas of the Neogene calc-alkaline volcanic rocks. 1 – Outer Carpathians (Moldavide), Neogene–Quaternary sediments, and flysch nappes; 2 – Pieniny klippe belt; 3 – Pre-Neogene rocks of the inner Alpine–Carpathian Mountains; 4 – Neogene calc-alkaline volcanic areas; 5 – Major thrusts; 6 – Strike-slip faults. (b) Geological sketch of the Cãlimani-Gurghiu-Harghita volcanic arc, Eastern Carpathians (adapted from Rãdulescu *et al.* 1973; Szakacs and Seghedi, 1995). (b) 1 – Upper structural compartment (central or 'core' and proximal or 'flank' facies model). The central (or core) facies is bounded by the present-day topographic rim of the enlarged central volcanic depressions consisting of the eroded central summit of the volcanoes with unroofed intrusive core complexes and related alteration halos, the crater and/or caldera remnants, and eruptive vents, whereas the proximal facies corresponds to lava-flow piles and subordinate pyroclastic interbeds which accompany the modified outer slopes of the volcanic edifices (Szakacs and Seghedi, 1995); 2 – lower structural compartment (peripheral distal or volcanoclastic facies model, which surrounds the base of volcanoes); 3 – crater area; 4 – centers of eruptions. The Harghita Bãi hydrothermal area is indicated by an arrow.

from the bottom of the BS gave an age of 4.5 Ma (Clauer *et al.*, 2010). Therefore, both illite minerals crystallized in the same space (inside and outside of the BS) at different geological times.

Mine drifts from −30 m, −50 m, and −80 m to −110 m, including mine shafts, were prospected in order to obtain information on the geometry, shape, and texture of the BS. The BS consists of irregular, hydraulically fractured blocks of argillized andesite, where NH_4-I formed in economic concentrations. The BS consists of fractured andesitic blocks (*in situ;* at ~−95 m) cemented by quartz, pyrite, and tourmaline, where the samples 138431 and HB-19 (NH_4-I; 5% S) were collected from the site shown in Figure 2.

Irregular, rounded, or elliptical andesitic clasts were observed at the top of the BS, suggesting that fragments and blocks of andesitic flow rose through the pipe as a result of gas explosions. No tuffaceous matrix or exotic rocks from the pre-volcanic fundament were identified within the breccia matrix. Andesitic blocks and angular or elliptical fragments were cemented by andesitic-flour material resulting from the gas explosion.

https://doi.org/10.1346/CCMN.2013.0610415 Published online by Cambridge University Press

Figure 2. Photo of a hydrothermal breccia structure showing argillic altered pyroxene andesitic blocks ('tobelitic' rocks) fractured *in situ*. The NH_4-I samples 138431 and HB-19 collected at −95 m (location in photo) correspond to the lognormal CTD shape.

Argillized rocks from Harghita Bãi area were commercially known in the last century as 'Kaolin of Harghita', and were exploited for the chemical and paper industries.

MATERIALS AND METHODS

Materials

The NH_4-I-bearing argillized andesite rocks were collected from the mine drifts and shafts located at depths of −30, −50, −80, and −110 m, where a broad 'tobelitization' zone occurs exceeding 80 m in depth. The 24 samples (NH_4-I-S) were collected from the different levels within the BS ('tobelitization' zone), whereas three other samples (K-I/NH_4-I mixtures) were taken from −110 m, outside of the BS. The samples collected were divided in two distinct groups: the first was related to the NH_4-I-S interstratified structures (30−5% S), whereas the second was related to K-I/NH_4-I mixtures. The corresponding number and expandability of each NH_4-I-S sample (both <2 μm and <2−0.2 μm fractions) selected for thickness measurements, are shown in Tables 1 and 2, whereas the expandability changes in the NH_4-I-S interstratified structures at each underground level along the hydrothermal breccia structure and the spatial relationship with K-I/NH_4-I mixtures are shown in Figure 14.

Sample preparation

The chemical treatments of the clay samples followed Jackson's (1975) techniques. The samples were treated

Table 1. Parameters of %S, T_{mean}, α, β^2, surface area, and crystallite-thickness distribution shapes of Li^+- and PVP-10-saturated NH_4-I-S interstratified structures and NH_4-I/K-I mixture phases (<2 μm and <2−0.2 μm clay fractions).

Sample	Depth (m)	%S	Surface area	α	β^2	T_{mean}	CTD shape	Nucleation + growth	Surface control
138442	−58	30	218	1.13	0.18	3.4	Asymp.	3	0
HB-4	−68	30	200	1.21	0.18	3.7	Asymp.	3	0
205	−70	30	248	1.04	0.12	2.8	Asymp.	2	0
138444	−68	30	153	1.44	0.27	4.8	Asymp.	3	0
HB-14	−75	20	179	1.32	0.21	4.1	Asymp.	3	0
138443	−68	20	140	1.47	0.37	5.3	Asymp.	5	0
HB-15	−79	15	162	1.42	0.20	4.6	Asymp.	3	0
138446	−85	10	142	1.35	0.23	4.3	Asymp.	3	0
138445	−85	10	125	1.65	0.27	5.8	Asymp.	4	0
HB-17	−85	10	119	1.74	0.17	6.2	Lognor.	2	3
352	−85	10	110	1.75	0.33	6.8	Lognor	4	1
340K	−95	5	195	1.22	0.22	3.9	Lognor	3	1
HB-19	−95	5	116	1.74	0.22	6.4	Lognor.	3	2
HB-18	−95	5	126	1.76	0.34	6.9	Lognor.	3	2
138555	−95	5	105	1.82	0.27	7.1	Lognor.	4	2
138444*	−68	30	164	1.38	0.24	4.6	Asymp.	3	0
138443*	−68	20	167	1.43	0.26	4.7	Asymp.	4	0
138446*	−85	10	183	1.30	0.19	4.1	Asymp.	3	0
138445*	−85	10	123	1.62	0.36	5.9	Lognor	3	2
138430*	−95	5	95	1.87	0.34	7.8	Lognor.	2	3
138431*	−95	5	122	1.65	0.28	5.9	Lognor	4	1
138340*	−95	5	114	1.81	0.21	3.7	Lognor	3	2
138426	−110	0	63	2.32	0.28	11.7	Bimodal	3	3
138426*	−110	0	–	1.93	0.43	8.7	Bimodal	4	2
HB-9	−110	0	95	1.85	0.36	7.8	Bimodal	4	2
138553	−110	0	78	2.05	0.41	9.6	Bimodal	5	3
Tobelite	Japan	0	55	2.39	0.37	21.5		4	3

* <2−0.2 μm clay fraction

https://doi.org/10.1346/CCMN.2013.0610415 Published online by Cambridge University Press

Table 2. Proportions of each illite phase in NH_4-I/K-I mixture phases calculated using the *UnMixer* code. Parameters of T_{mean}, α, β^2, and surface area of Li^+- and PVP-10-saturated NH_4-I/K-I mixture phases (<2 μm and <2−0.2 μm clay fractions) calculated using the *MudMaster* code.

Sample	Depth	Surface area	Proportion of (K-I)	Proportion of (NH_4-I)	α (NH_4-I)	β^2 (NH_4-I)	T_{mean} (NH_4-I)	α (I-K)	β^2 (I-K)	T_{mean} (K-I)	CTD
138426	−110	68	0.64	0.36	3.03	0.354	12.5	2.36	0.33	24.7	Bimod
138426*	−110	101	0.60	0.40	1.77	0.38	7.1	2.50	0.19	13.4	Bimod
HB-9	−110	121	0.53	0.47	1.60	0.22	5.5	2.54	0.50	16.2	Bimod
138553	−110	86	0.47	0.53	1.47	0.2	4.8	2.35	0.29	12.1	Bimod

* <2−0.2 μm clay fraction

with Na-acetate (NaOAc) to remove carbonate (pH = 5.5; T = 100ºC). Both Fe and Al (oxyhydr)oxides were removed using Na-dithionite and Na-citrate (pH = 7; $T \approx$ 80ºC). The salt excess was removed from the <2 μm clay fractions by washing in distilled water followed by dialysis. The samples were washed several times after saturation with each inorganic complex, in a 1:1 deioinized water:ethanol mixture, until chloride-free, based on the $AgNO_3$ test which confirmed the complete removal of Cl^- ions. The oriented clay-aggregate specimens were ethylene glycol (EG) solvated for 8 h at 60ºC.

The <2 μm size fraction was separated by successive dispersion and sedimentation cycles in distilled water according to Stoke's Law; the clay fractions were concentrated by centrifugation and re-dispersed with an ultrasonic probe. Then the <0.2 μm size fraction was extracted first from the <2 μm size fraction using continuous-flow ultra-centrifugation. The remaining <2−0.2 μm fraction was collected after the extraction of the <0.2 μm clay size fraction.

The <2 μm and <2−0.2 μm fractions of 27 selected samples of NH_4-I-S ordered mixed-layer series (R1, R2, R3), end-member NH_4-I, and NH_4-I/K-I mixture phases were Li saturated, mixed with aqueous solutions of PVP-10 (polyvinylpyrrolidone, MW = 10,000) to remove swelling (Eberl *et al.*, 1998b), and then hardened at 60 to 90ºC on polished Si-metal wafers. Li-saturated clay fractions were suspended in distilled water (concentration 2.5 mg clay/mL H_2O), and then mixed with an aqueous solution containing 5 mg PVP/mL H_2O. The mixtures were sonicated at low power using a Heat Systems-Ultrasonics, Inc. ultrasonic probe (QSonica, LLC, Newtowne, Connecticut, USA) for ~10−15 s, and then mounted on Si wafers for analysis by XRD.

X-ray diffraction

The XRD patterns of oriented specimens were obtained using a Rigaku Geigerflex D/max.-C series automated diffraction system (Tokyo, Japan) equipped with a graphite monochromator and using CuKα radiation. Samples were analyzed in the range 2−50º2θ, using a 1º divergence slit, a step size of 0.05º2θ, and a counting time of 5 s/step. The XRD patterns of oriented specimens were acquired in the range 2−35º2θ, using a Philips-PW 1710 diffraction system (Eindhoven, Holland) equipped with a diffracted-beam monochromator system, CoKα radiation (10 mA; 40 kV), a step size of 0.05º2θ, and a counting time of 5 s/step.

The Li-saturated and PVP-10-intercalated samples were analyzed by XRD using a Siemens D500 X-ray diffractometer (Karlsruhe, Germany) at the USGS, Boulder, Colorado, USA, also equipped with a diffracted-beam graphite monochromator and with two Söller slits, a 1º divergence slit, 1º and 0.6º receiving slits, CuKα radiation (30 mA; 40 kV), a step size of 0.02º2θ, and a count time of 20 s/step in the range 2−50º2θ. The same setup was used for an instrumental broadening standard, NBS 676 (alumina powder).

Estimation of the smectite content (%S)

The %S for NH_4-I-S selected samples was estimated using the *NEWMOD*© computer program (Reynolds, 1985).

Bertaut-Warren-Averbach (BWA) analysis

The 001 XRD peak for illite was analyzed for T_{mean} and CTD using the BWA method (Drits *et al.*, 1998) by means of the *MudMaster* code (Eberl *et al.*, 1996). The BWA calculations use the raw XRD data, where swelling was removed by PVP-10 intercalation. The 001 reflection of illite was influenced little by strain broadening and had a large intensity. However, the shape of the 001 reflection was more affected by LpG^2 (Lorentz polarization factor × the layer scattering intensity) than were the shapes of some higher-order reflections. The effect of LpG^2 was removed using the calculation method applied by Eberl *et al.* (1998b).

The programs *PeakChopper* and *UnMixer*, which are associated with the *MudMaster* package (Eberl, 2002), were used to remove the 001 reflection of chlorite and to quantify the proportion of each illite component in NH_4-I and K-I mixture phases. The distribution of each component was normalized to a constant volume, where volume-weighted frequencies were calculated by

https://doi.org/10.1346/CCMN.2013.0610415 Published online by Cambridge University Press

multiplying the area-weighted frequency by crystal thickness for each thickness class (Eberl, 2002).

Simulating the shape of the crystal-size distribution

The computer program *Galoper* (Eberl *et al.*, 2000) was used to simulate the shapes of CTDs in order to interpret crystal-growth mechanisms. The Kolmogorov-Smirnov (K-S) statistical test (Benjamin and Cornell, 1970) and the Chi-square test (χ^2; Krumbein and Graybill, 1965) were used to compare *Galoper*-simulated and *MudMaster*-measured CTDs. These tests give a level of significance for matching the shapes of the CTDs, from <1% (not significant) to >10% or >20% (high level of significance).

Thickness measurement

Crystal-thickness distribution, mean thickness extrapolated from the Fourier coefficients ('best mean'), mean thickness calculated from the distribution, mean of the natural logarithms of coherent scattering domain thickness (α), and the variance of the logarithms of coherent scattering domain thickness (β^2) were calculated. Distributions of particle thicknesses were analyzed as (001) area-weighted (AW) and volume-weighted (VW) frequencies.

Scanning electron microscopy.

Scanning electron microscopy (SEM) was carried out using an Hitachi S-4100 electron microscope (Tokyo, Japan), equipped with an X-ray energy-dispersive spectral (EDS) spectrometer (Oxford Instruments INCA energy). The rocks were crushed into small pieces (5−8 mm in diameter), and, to preserve the textural morphology of the clay, the critical-point drying method was used (McHardy and Birnie, 1987). The samples were mounted on a carbon holder and sputter-coated with a thin carbon film.

RESULTS

Characterization of the XRD patterns of oriented clay-aggregate specimens

Samples were divided in two groups: one group corresponding to the NH_4-I-S interstratified structures (<2 μm and <2−0.2 μm clay fractions) and another to the NH_4-I/K-I mixture phases (<2 μm and <2−0.2 μm clay fractions). Clay fractions were Li saturated and then PVP-10 was sorbed to their surfaces to remove swelling. Lithium is more effective than Na^+ at dispersing high-charge smectite layers and PVP-10 prevents fundamental illite particles from undergoing interparticle diffraction (Eberl *et al*., 1998). Swelling tends to broaden XRD peaks and, therefore, interferes with crystallite-thickness measurements based on peak shape.

NH_4-I-S interstratified structures (<2 μm clay fractions). The XRD patterns of NH_4-I-S spanned a wide Reichweite (R) ordering (R1, R2, and R3), and ranged from 30 to 5% S (Figure 3). The *NEWMOD* program was used to estimate the %S and to verify the NH_4-I-S structural behavior in the AD and EG states (Bobos, 2012). The best model obtained suggests that NH_4-I was interstratified with two-water (2W) or one-water layer smectite (1W). The 005 values shifted from 2.02 Å to 2.048 Å as the amount of NH_4^+ increased in illite layers. The full width at half maximum (FWHM) intensity of the 001 peak in AD ranged from 0.3 (5% S) to 0.37 (10% S) and 0.42 (15% S) º2θ (CuKα). The samples with low %S values had a narrow and symmetrical 001 peak, consisting of thicker NH_4-I crystals, whereas the samples with large %S values had a large FWHM ($\geqslant$0.4, º2θ CuKα). The NH_4^+ and K^+ were distributed homogeneously in the illite interlayers, and the K^+ content was <0.1 equivalents per $O_{10}(OH)_2$ (Bobos, 2012).

NH_4-I-S interstratified structures (<2−0.2 μm clay fractions). Samples selected from this size fraction behaved in a similar manner to 2WS-NH_4-I and 1WS-NH_4-I, where the %S content ranged from 30 to 5%. The XRD patterns were obtained over the range 2−35º2θ CoKα (Figure 4). The XRD patterns confirmed the same range of ordering and %S shown previously for the <2 μm clay fractions. The 005 peak occurred at 2.034 Å for samples 138444 and 18443 and at 2.038 Å for samples 138446 and 138445. The amounts of K^+ for the selected samples (<2−0.2 μm clay fractions) were <0.1 equivalents per $O_{10}(OH)_2$ (Bobos, unpublished data).

The 00l peaks corresponding to the <2−0.2 μm clay fractions showed different positions from those obtained for the <2 μm clay fractions (Figure 3), because the samples were analyzed in a lab with low humidity (<20% RH). The positions and amount (H_2O and EG molecules) of interlayer species were considered to be variable parameters (Moore and Reynolds, 1997).

NH_4-I/K-I mixture phases (<2 μm clay fractions). The XRD patterns of samples HB-9, 138426, and 138553 exhibited changes in the resolution and the position of the 00*l* reflections (Figure 5a). The positions of the 001, 004, and 005 reflections were very sensitive to the structural characteristics of these mixed phases. The 001 peak was relatively sharp (narrow peak width) and no changes were observed in two of the samples after EG solvation. However, the 001 peak of sample HB-9 expanded from 10.40 to 10.60 Å after EG solvation, suggesting a few smectite layers interstratified with NH_4-I. For all three samples, two distinct peaks for the 004 reflection were observed at 2.50 Å and 2.57 Å, whereas the 005 peak occurred at 2.00 Å with a shoulder at 2.03 Å (Figure 5a,b). Both peaks were well defined after decomposition of the 005 reflection corresponding to an XRD pattern of sample HB-9 (Figure 5c).

Thus, the XRD patterns of the NH_4-I/K-I mixture phases showed two distinct *d* spacings for the 001, 004,

https://doi.org/10.1346/CCMN.2013.0610415 Published online by Cambridge University Press

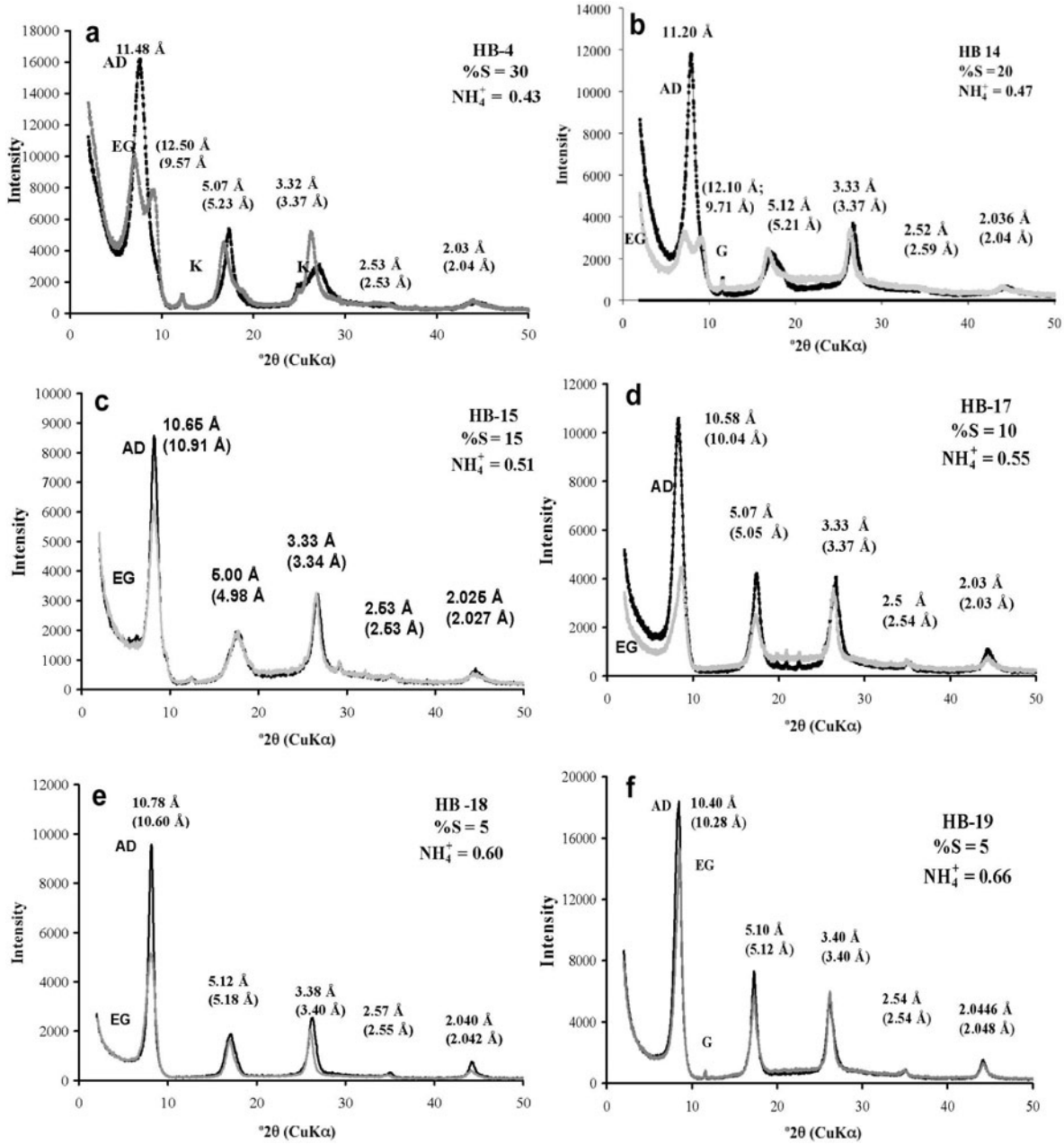

Figure 3. Selected XRD patterns of NH_4-I-S interstratified structures from oriented specimens (<2 μm clay fraction) used subsequently for the BWA analysis (AD – air-dried: black lines; EG – ethylene-glycol solvated: gray lines). K – kaolinite; G – gypsum.

and 005 peaks. This interpretation was verified by mixing two *NEWMOD*©-calculated patterns (K-I + NH_4-I). The XRD patterns were modeled using *NEWMOD*© by adding *MIXER* and *MIX* accessory data files. The present authors assumed that only NH_4^+ is fixed in NH_4-I interlayers, whereas the K^+ occurs in K-I interlayers. The result was a *MIX* data file corresponding to a physical mixture of NH_4-I and K-I in equal proportions. The CuKα intensity of NH_4-I was greater than that of K-I in the selected samples even if the proportion of K-I was greater relative to NH_4-I. Mixing the two calculated XRD patterns of K-I and NH_4-I (Figure 5d) confirmed the experimental data obtained for NH_4-I/K-I mixtures.

Li- and PVP-10-saturated samples. Mixed layering affects the peak shapes by broadening them; therefore, these peaks were not suitable for crystallite-thickness measurements. After Li saturation and PVP-10 intercalation, the samples could behave as a mixed-layer

https://doi.org/10.1346/CCMN.2013.0610415 Published online by Cambridge University Press

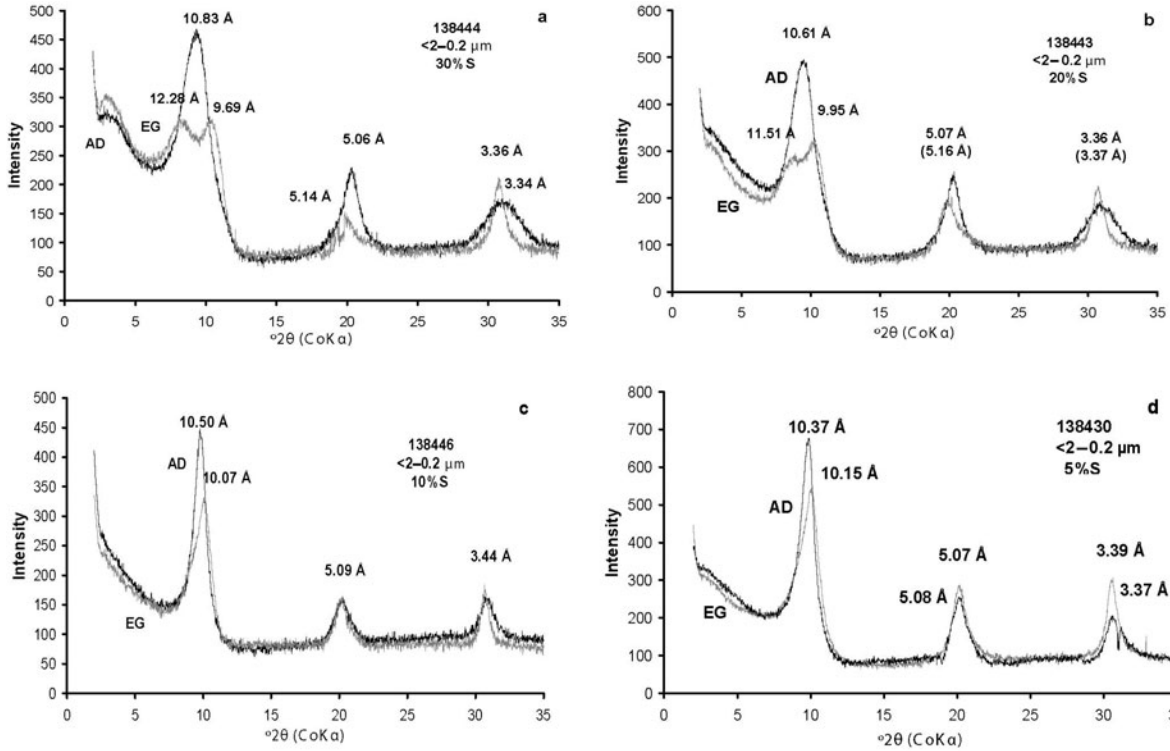

Figure 4. Selected XRD patterns of NH_4-I-S interstratified structures from oriented specimens (<2−0.2 μm clay fractions) used subsequently for the BWA analysis (AD: black lines; EG: gray lines).

structure consisting of 10.33 Å and 9.98 Å layers, depending on the proportion of NH_4-I and K-I interlayers. However, the XRD patterns obtained after Li-saturation and PVP-10 intercalation showed 00*l* reflections corresponding to end-member NH_4-I. The 001 peak of NH_4-I-S sample HB-2 (40% S) was broad and had a very high peak-intensity ratio of the low-angle saddle/001 after Li and PVP-10 saturation. Therefore, the present sample, described by Bobos (2012), was rejected, and only the NH_4-I-S samples with <30% S were used for thickness measurements (Figure 6). The 001 reflections of NH_4-I-S interstratified structures (<2 μm clay fractions, <20% S) showed a sharp peak at ~10 Å, and the position of the 005 basal reflection shifted toward lower angles after PVP treatment. The XRD patterns of NH_4-I-S (<2−0.2 μm clay fractions) showed greater intensities (Figure 6) for the 00l reflections than those obtained for the <2 μm clay fractions.

Several selected samples of NH_4-I-S interstratified structures (*i.e.* 138446 and 138445) contained impurities (*i.e.* chlorite at 14 Å) identified in the XRD patterns. These unwanted peaks, found in the tails of 001 peaks corresponding to NH_4-I, were removed using the *PeakChopper* code (Eberl, 2002) by drawing a line along the background through the base of the peak. However, the effect of neighboring peaks was insignificant because the accessory phase was present in a proportion <0.5 (Eberl *et al.*, 2003).

The XRD profiles of the NH_4-I/K-I mixed samples showed a pattern typical of K-I. However, the 005 reflection at 2.00 Å exhibited the same shoulder at 2.03 Å (NH_4-I) described previously for samples that were not treated with Li and PVP-10. The 004 reflection showed two distinct peaks at 2.50 Å and 2.57 Å. Changes in the intensity of 002 and 003 reflections were comparable with the same reflections in relation to NH_4-I-S interstratified structures.

Morphology

Ammonium-illite exhibited an oriented lath-shaped morphology with variable width along the *a** direction. Two populations with illite aggregates were observed in sample HB-9: one consisting of relatively oriented laths (NH_4-I), apparently having the same widths, and the other of small pseudohexagonal platy aggregates of K-I (Figure 7a). The lath-shaped crystals of NH_4-I (5%, sample HB-18) were well defined with lengths of 6−10 μm (Figure 7b).

The thickness of NH_4-I crystals estimated by the BWA method

NH_4-I-S interstratified structures. The CTDs of ordered NH_4-I−S (30, 20, 15, and 10% S) mixed-layers (<2 μm clay fractions) displayed an asymptotic shape (Figure 8a), whereas the end-member NH_4-I (5% S) had a lognormal shape (Figure 8b). The experimental

https://doi.org/10.1346/CCMN.2013.0610415 Published online by Cambridge University Press

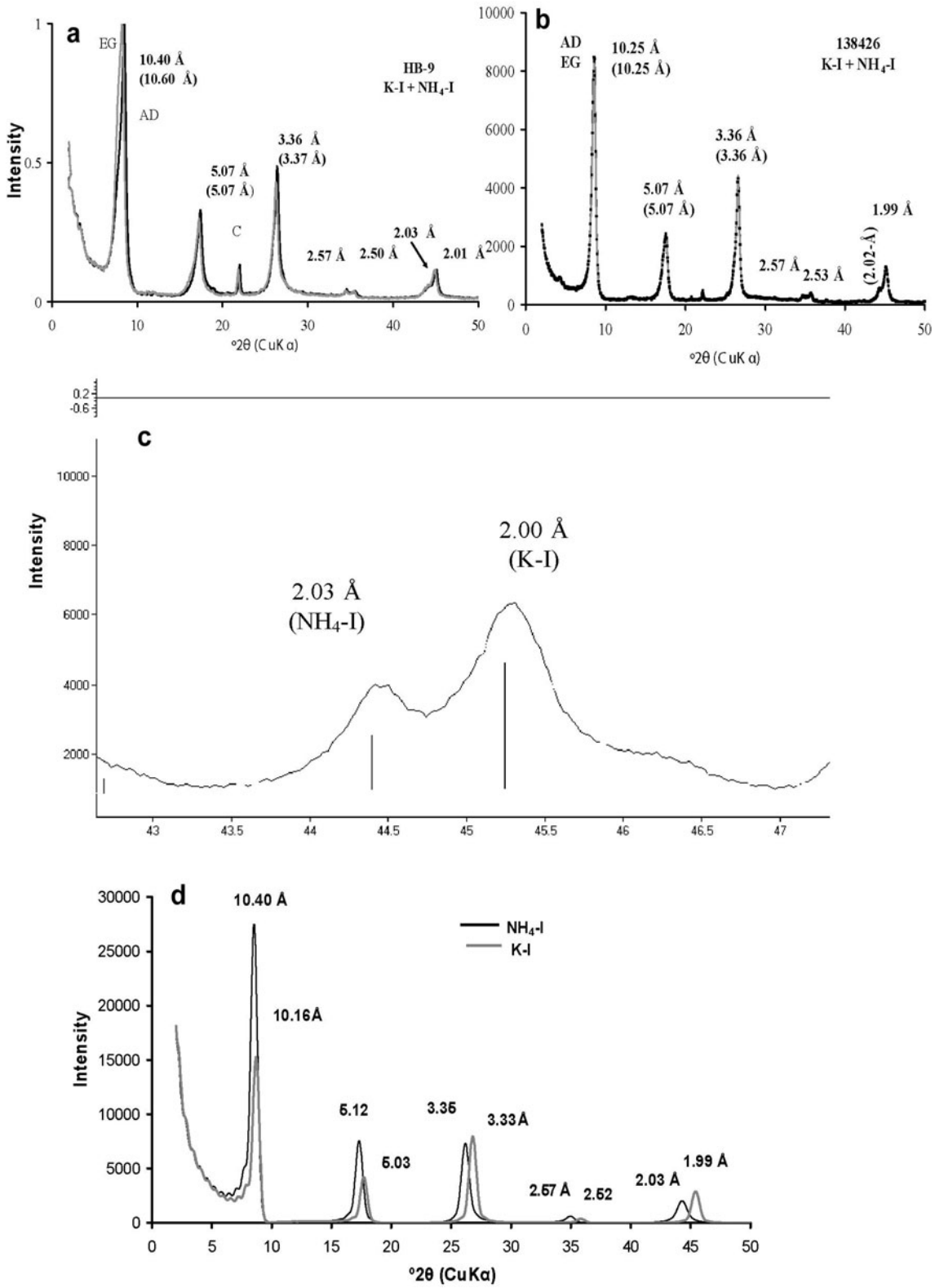

Figure 5. Selected XRD patterns of NH_4-I/K-I mixture phases (a,b) from oriented specimens (<2 μm clay fractions) used subsequently for BWA analysis (AD: black lines; EG: gray lines). C – cristobalite. (c) Decomposition of the 005 peak corresponding to NH_4-I/K-I mixture phases of sample HB-9. (d) XRD pattern of NH_4-I/K-I mixed phases simulated by the *NEWMOD* code by adding *MIXER* and *MIX* accessory data files.

https://doi.org/10.1346/CCMN.2013.0610415 Published online by Cambridge University Press

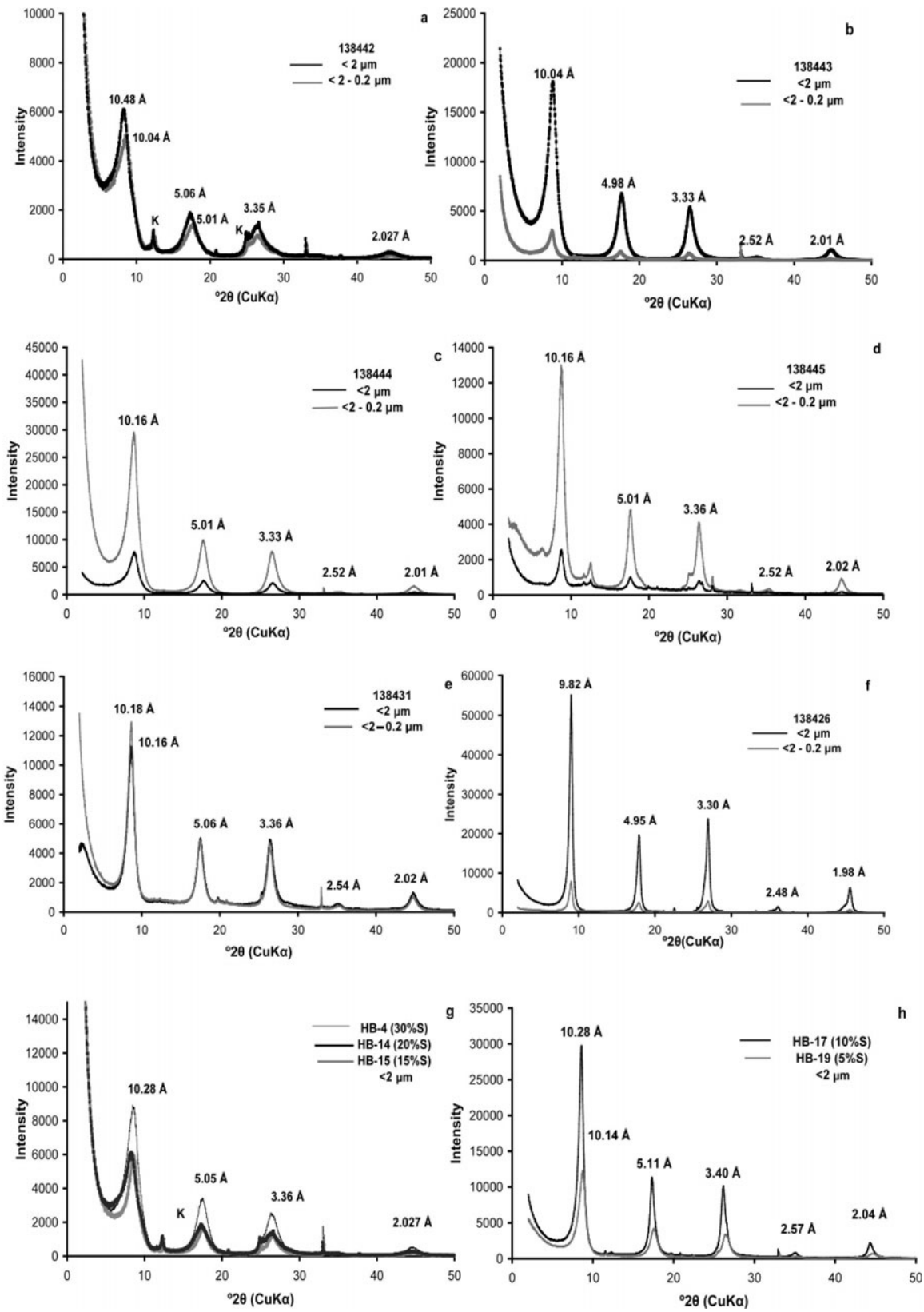

Figure 6. Selected XRD patterns of Li^+-saturated and PVP-10-intercalated NH_4-I-S interstratified structures and NH_4-I/K-I mixture phases from oriented specimens used for BWA analysis.

https://doi.org/10.1346/CCMN.2013.0610415 Published online by Cambridge University Press

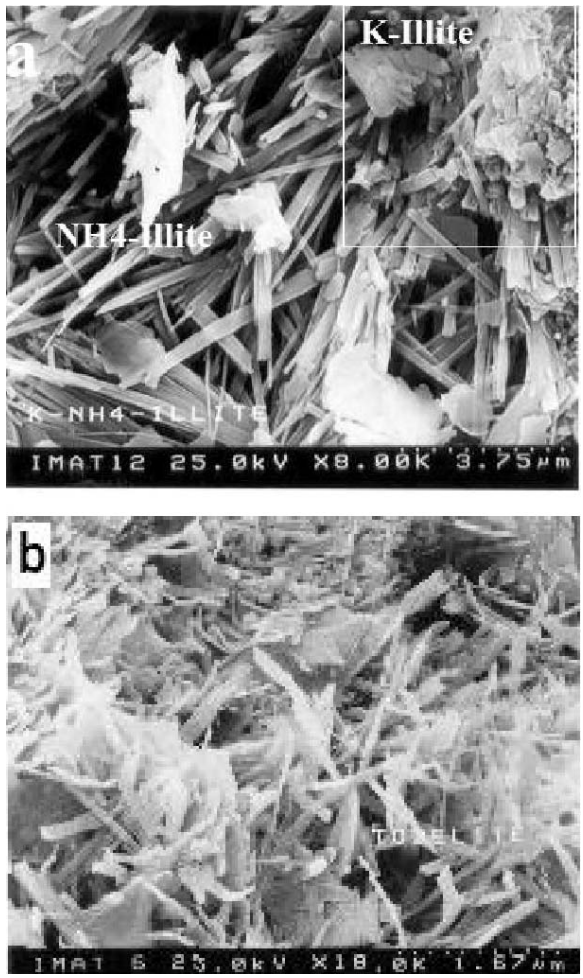

Figure 7. SEM images of (a) NH_4-I/K-I mixture phases and (b) NH_4-I. The NH_4-I exhibits a lath-shaped morphology whereas the K-I shows small pseudohexagonal platy aggregates.

T_{mean} of NH_4-I-S crystallites (30−5% S) ranged from 3.4 to 7.1 nm. The CTD shapes of ordered mixed layer NH_4-I-S (30−10% S) corresponding to the <2−0.2 µm fractions were also asymptotic (samples 138444, 138443, 138445, and 138446), where the T_{mean} ranged from 4.1 nm to 5.9 nm. Samples 138431 and 138430 (5% S) exhibited a lognormal-like shape, where the T_{mean} ranged from 5.9 to 7.8 nm. The T_{mean}, α, β^2, and surface area (Table 1) corresponding to selected samples were calculated using the *MudMaster* code.

NH_4-I/K-I mixture phases. Calculation of the proportions of NH_4-I and K-I using the UnMixer code. The CTD shapes for NH_4-I/K-I mixture phases (both <2 µm and <2−0.2 µm clay fractions) were neither asymptotic nor lognormal, but were probably bimodal (Figure 9a), composed of the sum of two lognormal-like shapes (Figure 9b). Two lognormal distributions for NH_4-I/K-I mixture having different proportions were obtained using the *UnMixer* code.

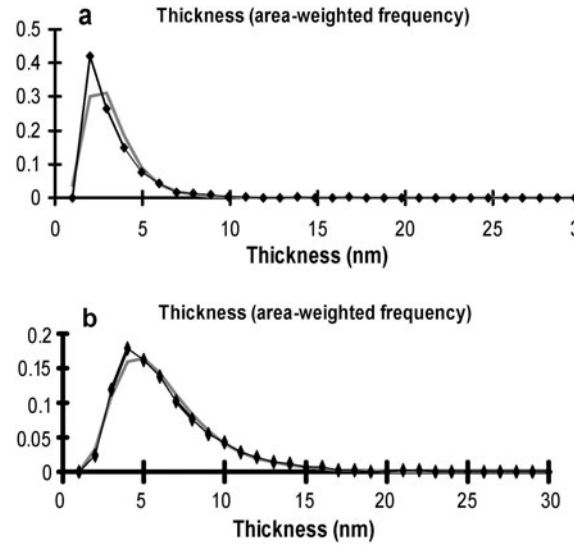

Figure 8. (a) Asymptotic CTD shape of NH_4-I (sample 138342). (b) Lognormal CTD shape of the end-member NH_4-I sample (sample 138431; <2 µm clay fraction). Solid curves are theoretical lognormal curves calculated from the data obtained.

The proportion of K-I ranged from 0.47 to 0.64 and the NH_4-I ranged from 0.53 to 0.36 in the <2 µm clay fractions, whereas the NH_4-I/K-I ratio in the <2−0.2 µm clay fraction for sample 138426 was 0.40/0.60 (Table 2). The T_{mean} measured for NH_4-I ranged from 4.8 nm to 12.5 nm and from 12.1 to 24.7 nm for K-I. The parameters for T_{mean}, α, β^2, and surface area were calculated using the *MudMaster* code (Table 2).

Crystal-growth mechanisms from crystal-thickness distribution shapes (Galoper code)

Crystal-growth mechanisms that gave rise to the shapes of NH_4-illite CTDs can be deduced for a sample by plotting the natural log of the mean crystal thickness (α) and its variance (β^2) on an α–β^2 diagram (Bove *et al.*, 2002), where $\alpha = \sum \ln(T) f(T)$, $\beta = \sum (T - \alpha)^2 f(T)$, and $f(T)$ refers to frequency of the occurrence of a given crystal thickness. Values obtained (Table 1) were plotted on an α–β^2 diagram (Figure 10) constructed using *Galoper* calculations for the crystal-growth mechanisms of simultaneous nucleation and growth, and for surface-controlled growth without simultaneous nucleation. The numbers of simultaneous nucleation-plus-growth cycles and growth-only cycles were calculated for the samples analyzed (Table 1).

Curve A−B (Figure 10) was followed by illites undergoing simultaneous nucleation and growth. Each dot (labeled 1 through 6) on this curve represents a new nucleation event, which occurred at the same time as previously nucleated crystals grew by the law of proportionate effect (LPE; Eberl *et al.*, 1998a). Illites following this reaction path yielded an asymptotically shaped CTD. Samples HB-4 (30% S), 138442 (30% S), and 138443 (20% S) lay along the path A−B, where the

https://doi.org/10.1346/CCMN.2013.0610415 Published online by Cambridge University Press

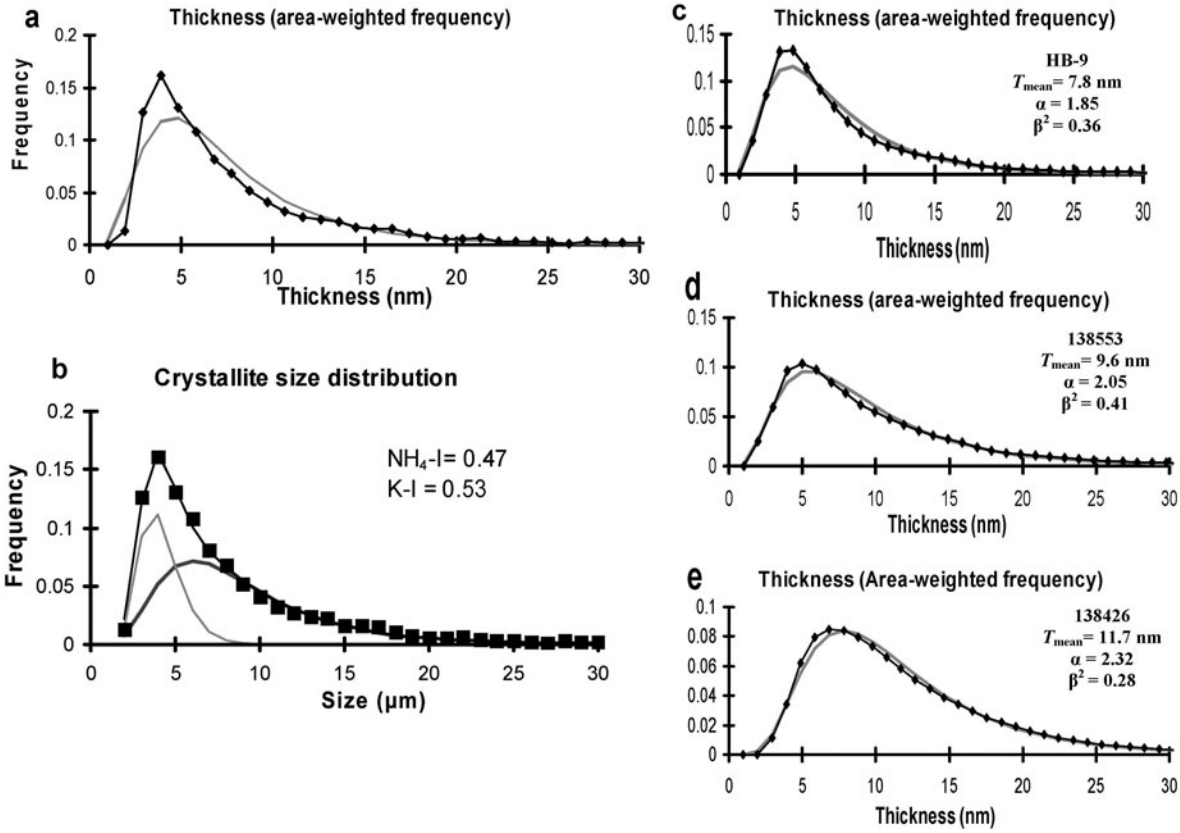

Figure 9. Bimodal-like CTD shape of NH_4-I/K-I mixture crystallites (sample HB-9). (a) The bimodal shape distribution and superposition of two lognormal distribution shape models. (b) Decomposition of the bimodal-like shape distribution of NH_4-I/K-I mixture crystallites using the *UnMixer* code. (c, d, e) Lognormal distribution shapes of NH_4-I obtained from NH_4-I/K-I mixture crystallites (samples HB-9, 138553, and 138426). The T_{mean} ranges from 7.8 to 11.7 nm.

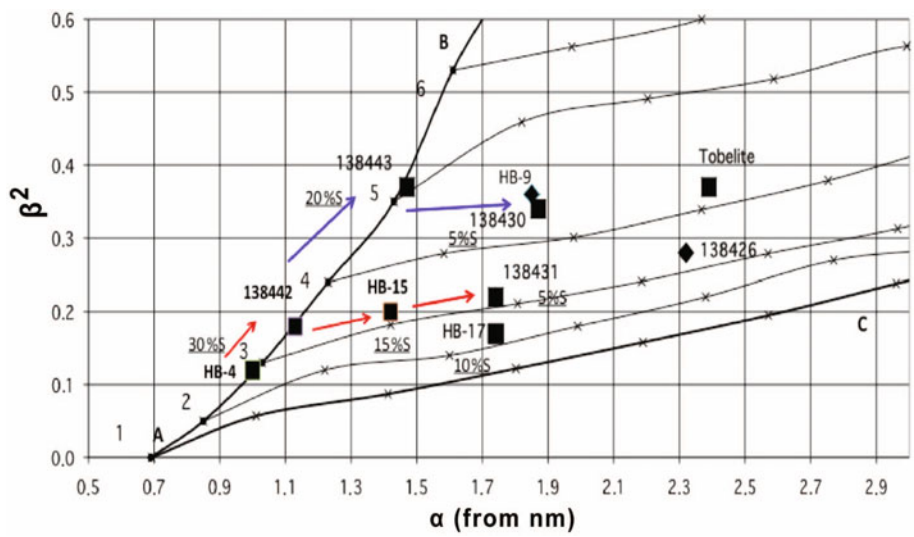

Figure 10. Parameters of NH_4-I from NH_4-I-S interstratified structures and NH_4-I/K-I mixture phases plotted in α–β^2 diagrams. The reaction path of NH_4-I (<2 μm clay fraction) simulates constant-rate nucleation and growth (samples HB-4, 138442, and 138443) followed by surface-controlled growth (samples 138430 and 138431). The NH_4-I from NH_4-I/K-I mixture phases and tobelite (Japan) also underwent simultaneous nucleation and growth followed by LPE surface-controlled growth (see explanation in text). The NH_4-I corresponding to the <2−0.2 μm clay fraction also accompanies the reaction path of NH_4-I corresponding to the <2 μm clay fractions.

https://doi.org/10.1346/CCMN.2013.0610415 Published online by Cambridge University Press

CTDs were simulated with *Galoper* using 3 (HB-4), 4 (138442), and 5 (138443) nucleation-and-growth cycles (the samples corresponding to the <2−0.2 μm clay fractions accompanied the <2 μm clay fractions). The simultaneous constant-rate nucleation and growth mechanism gave the asymptotic CTD shape (Figure 11a). The fit between the simulated and the measured CTD was verified by using either the Kolmogorov-Smirnov (K-S) or the Chi-squared statistical tests. The significance levels found for these samples varied from <1% (sample HB-4) where the statistical fit was not significant (but looks close), to 1−5% (sample 138442), to >10% (sample 138443).

Curve A−C (Figure 10) assumed that all crystals nucleated simultaneously and then grew by the LPE. Growth along this curve yielded a lognormal CTD, where each 'X' on the curve represents another growth cycle by the LPE.

Most of the samples depicted in Figure 10 lay between curves A−B and A−C. The reaction paths for these CTDs followed curve A−B until nucleation ceased, and then followed one of the curves that are parallel to A−C. Samples HB-15 (15% S), HB-17 (10% S), and 138431 (5% S) lay above the A−C curve. Sample HB-15 was simulated by having three nucleation-and-growth cycles followed by one growth cycle. The CTD shape obtained by BWA analysis was asymmetric. The CTD of sample HB-17 was best simulated by having three nucleation-and-growth cycles followed by two growth cycles without simultaneous nucleation (Figure 11b). The CTD of sample 138431 (5% S) was simulated by three nucleation-and-growth cycles, followed by two growth cycles without simultaneous nucleation (Figure 11c). The CTD for sample 138430 was simulated assuming four nucleation-and-growth cycles followed by two growth cycles without nucleation. The CTD of sample HB-9 (Figure 11d) was best simulated by assuming four cycles of nucleation and growth, followed by two growth cycles without simultaneous nucleation. Sample 138426 required three nucleation-and-growth cycles and three growth cycles without nucleation. The level of significance in the K-S test was >10%.

The XRD pattern of the Li-saturated and PVP-intercalated tobelite sample (Tobe mine, Japan; Higashi 1982) and the CTD were simulated using the *Galoper* code (Figure 12). The tobelite sample lay in the region between paths A−B and A−C in Figure 10. Simulation of its CTD required four nucleation-and-growth cycles, followed by three growth cycles without nucleation, where the level of significance in the Chi-squared analysis was >20%.

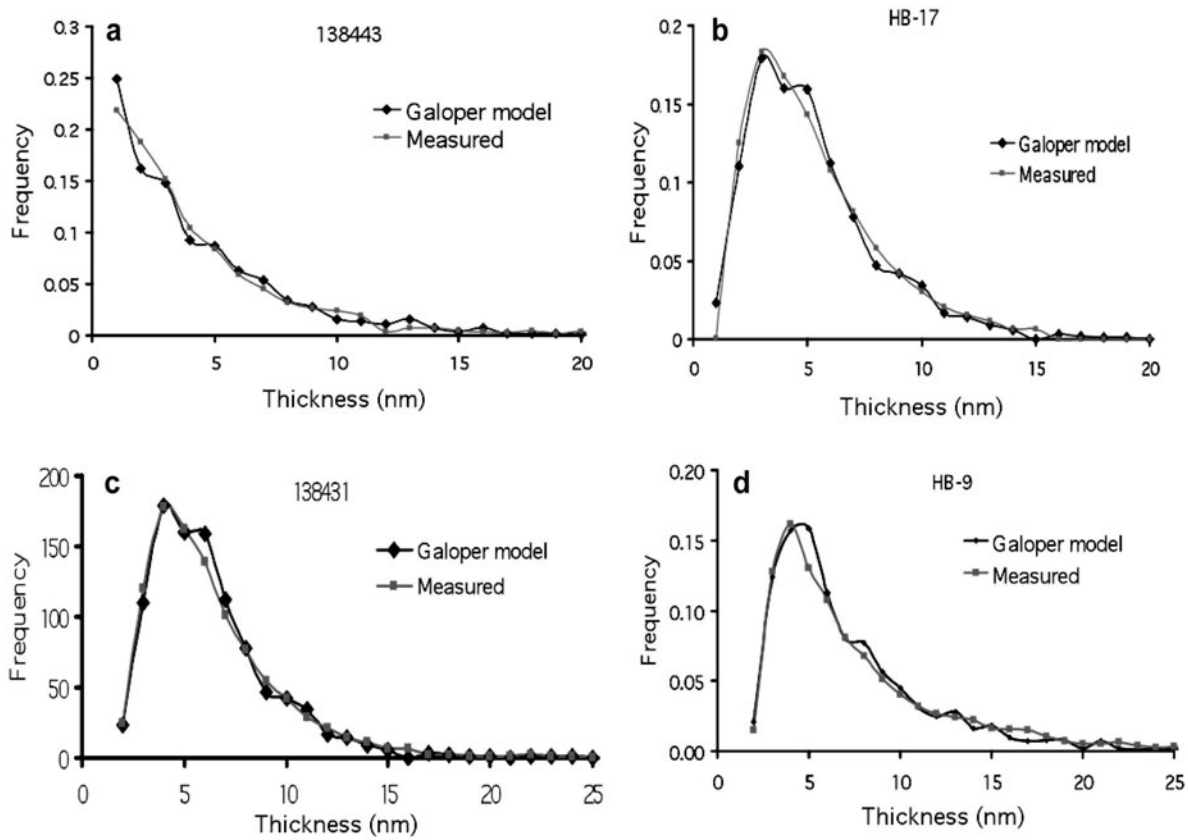

Figure 11. The CTD shapes of samples (a) 138443, (b) HB-17, (c) 138431, and (d) HB-9 simulated using *Galoper* code (explanation in text).

https://doi.org/10.1346/CCMN.2013.0610415 Published online by Cambridge University Press

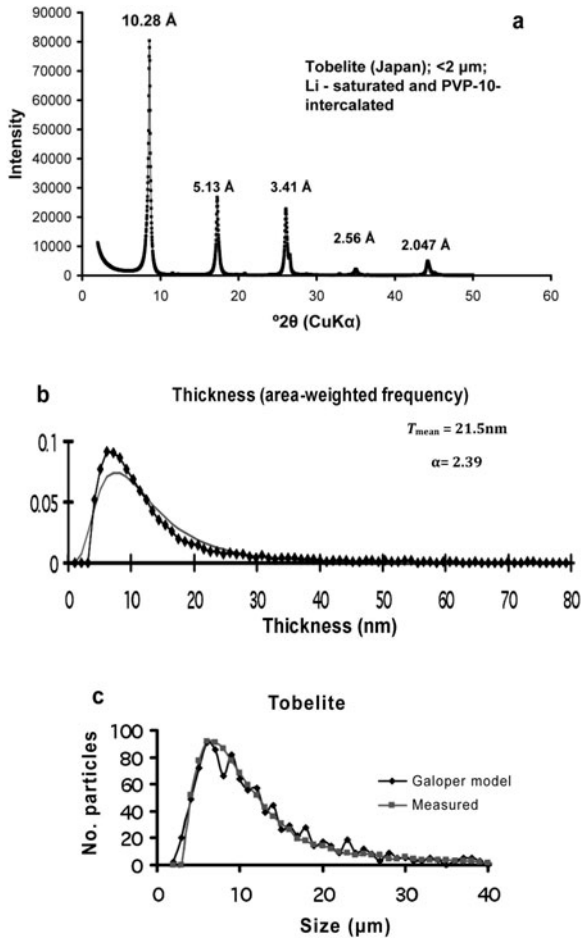

Figure 12. (a) XRD pattern of Li- and PVP-treated tobelite sample from Japan; (b) its crystallite thickness distribution; and (c) the *Galoper* simulation.

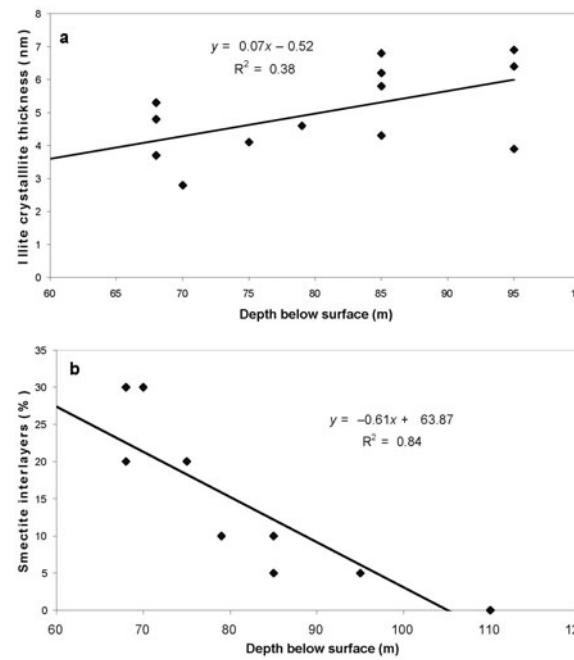

Figure 13. (a) Change in crystallite thickness distributions of NH_4-I (<2 μm) with depth, and (b) change in the %S layers with depth.

Application of the CTD measurements to the geological evolution of the Harghita Bãi hydrothermal system

In general, the zonality of hydrothermal alteration often occurs from an illite zone (phyllic) at the center of a deposit, to a smectite zone (propylitic) at the margin, where such zonation represents the effects of higher-temperature hydrothermal fluids at the center, and this zone sometimes contains metals (Inoue *et al.*, 1992). In the present study, the BWA technique applied to NH_4-I clays indicated a weak correlation in mean crystallite thickness with depth for NH_4-I (<2μm; Figure 13a), and a better correlation for NH_4-I-S with %S layers (Figure 13b). Changes in the T_{mean} of NH_4-I-S (30 to 5% S) from 2.8 nm to 7.1 nm for the <2 μm fractions were observed from −55 to −94 m (Figure 14). NH_4-I found at ~−94 m in the hydraulically fractured breccia (Figure 2) displayed a lognormal CTD shape.

Larger meteoric-hydrothermal breccias in porphyry Cu systems resulting from flashing of relatively cool groundwaters on approach to magma are usually related to late-mineral porphyry dikes, which may display downward transition to porphyry intrusions (Sillitoe, 2010). In most cases, the hydrothermal breccias are blind structures, which penetrate the overlying low- to high-sulfidation environment. Thus, the BS penetrated the phyllic and propylitic alteration envelopes in the Harghita Bãi area. Increasing the T_{mean} of NH_4-I in the phyllic (K-I) zone with increase of Zn^{2+} and Cu^{2+} concentration was well corroborated with the nitrogen increases in the hydrothermal system of Harghita Bãi (Bobos, 2000). Thus, the NH_3 was one of the most common ligands in solution, where metal complexes with four co-ordination may form either tetrahedral structures (*e.g.* in the case of Cu^{2+}) or square planar structures (*e.g.* in the case of Zn^{2+}) (Masterton *et al.*, 1981). Larger amount of metals than those surrounding stockwork mineralization could reflect the permeability of the BS.

Changes in mean illite particle thickness with depth were also identified in the Lake City caldera hydrothermal system (Colorado, USA), where the lognormal CTD shape was found in fractures and the asymptotic CTDs shape in wall rocks (Bove *et al.*, 2002). The lognormal CTD shapes coincided with major through-fractures or stockwork zones described elsewhere (Eberl *et al.*, 1987; Inoue and Kitagawa, 1994).

CONCLUSIONS

The mixed layering of illite with smectite arises from the stacking of NH_4-I crystals with smectite interlayers formed within the stacks at basal crystal interfaces. The

https://doi.org/10.1346/CCMN.2013.0610415 Published online by Cambridge University Press

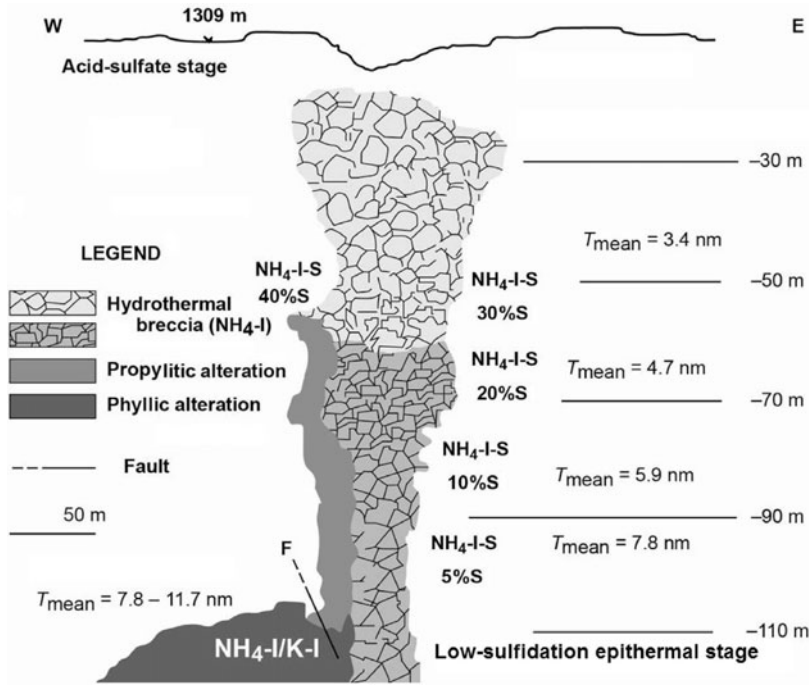

Figure 14. The distribution of NH_4-I samples (taking into account the %S) along the hydrothermal breccia structure (from −50 m to −110 m), and the relationship with K-illite (phyllic) and propylitic alteration. F: fault.

crystal growth history of the NH_4-I was elucidated using measurements of crystal thicknesses and by analyses of the shapes of CTDs. Many of the CTDs of NH_4-I have asymptotic shapes that result from simultaneous nucleation and growth. This shape evolves toward a lognormal shape when nucleation ceases but growth continues at levels of supersaturation that are too small to induce continued nucleation. The most evolved sample, found for the lognormal end-member NH_4-I, was found deep within the fractured BS, whereas the asymptotic shape was found within altered wall rock that is distal to zones of fractured hydrothermal breccia structure. Illite crystals in the fractured zone experienced greater water/rock ratios and, therefore, smaller levels of supersaturation than illite in the wall-rock. The more open environment of the fractured zone, combined with the elevated effects of temperature and pressure, contributed to a shorter nucleation stage and to a longer growth-only stage, leading to lognormal shapes for the CTDs.

ACKNOWLEDGMENTS

The authors are grateful to the International Office of the US Geological Survey which welcomed the first author as a Visiting Exchange Scholar during periods of sabbatical leave. Thanks to Alex Blum for fruitful and exciting discussions and to Prof. S. Higashi who supplied a tobelite sample from Tobe (Japan). The authors thank Prof. Joe Stucki (Editor-in-Chief) for his editorial handling and suggestions, and Prof. Warren Huff and the anonymous reviewers for thorough reading and helpful suggestions.

REFERENCES

Aldega, A. and Eberl, D.D. (2005) Detrital illite crystals identified from crystallite thickness measurements in siliciclastic sediments. *American Mineralogist*, **90**, 1587–1596.

Amelincks, S. (1952) La croissance helicoidale de cristaux du biotite. *Compte Rendu* Academie de Science Paris, **234**, 971–973.

Baronnet, A. (1982) Ostwald Ripening: The case of calcite and mica: *Estúdios Geologie*, **6**, 675–685.

Baronnet, A. (1984) Growth kinetics of the silicates. A review of basic concepts. *Fortschritte der Mineralogie*, **62**, 187–232.

Benjamin, J.R. and Cornell, C.A. (1970) *Probability and Decision for Civil Engineers*. McGraw-Hill, New York, 684 pp.

Bleahu M., Boccaletti, M., Manetti, P., and Peltz, S. (1973) Neogene Carpathian Arc: A continental arc displaying the features of an "Island Arc". *Journal of Geophysical Research*, **788/23**, 5025–5032.

Blum, A. (1994) Determination of illite-smectite particle morphology using scanning force microscopy. Pp. 171–202 in: *Scanning Probe Microscopy of Clay Minerals* (K.L. Nagy and A. Blum, editors). The Clay Minerals Society, Bloomington, Indiana, USA.

Bobos, I. (2000) The fossil hydrothermal system of Harghita Bãi, East Carpathians, Romania: Argillic alteration. Mineralogy, geochemistry and metallogeny. PhD thesis, Univ. Porto, Portugal, 174 pp. (in English).

Bobos, I. (2012) Characterization of smectite to NH_4-illite conversion series in the fossil hydrothermal system of Harghita Bãi, East Carpathians, Romania. *American Mineralogist*, **97**, 962–982.

Bobos, I. and Ghergari, L. (1999) Conversion of smectite to ammonium illite in the hydrothermal system of Harghita Bãi, Romania: SEM and TEM investigations. *Geologica Carpathica*, **50**, 379–387.

https://doi.org/10.1346/CCMN.2013.0610415 Published online by Cambridge University Press

Bove, D.J., Eberl, D.D., McCarty, D.K., and Meeker, G.P. (2002) Characterization and modeling of illite crystal particles and growth mechanisms in a zoned hydrothermal deposit, Lake City, Colorado. *American Mineralogist*, **87**, 1546–1556.

Brime, C. and Eberl, D.D. (2002) Growth mechanisms of low-grade illites based on shapes of crystal thickness distributions. *Schweizeriche Mineralogische Petrographische Mitteilungen*, **82**, 203–209.

Clauer, N., Liewig, N., and Bobos, I. (2010) K-Ar, $\delta^{18}O$ and *REE* constraints on the genesis of ammonium illite from the Harghita Bãi hydrothermal system, Romania. *Clay Minerals*, **45**, 393–411.

Drits, V., Eberl, D.D., and Środoń, J. (1998) XRD measurement of mean thickness, thickness distribution and strain for illite and illite-smectite crystallites by the Bertaut-Warren-Averbach technique. *Clays and Clay Minerals*, **46**, 38–50.

Dudek, T. and Środoń, J. (2003) Thickness distribution of illite crystals in shales. II: Origin of the distribution and the mechanism of smectite illitization in shales. *Clays and Clay Minerals*, **51**, 529–542.

Dudek, T., Środoń, J., Eberl, D.D., Elsass, F., and Uhlik, P. (2002) Thickness distribution of illite crystals in shales. I: X-ray diffraction *vs*. high resolution transmission electron microscopy measurements. *Clays and Clay Minerals*, **50**, 562–577.

Eberl, D.D. (2002) Determination of illite crystallite thickness distributions using X-ray diffraction, and the relation of the thickness to crystal growth mechanisms using MUDMASTER, GALOPER, and associated computer programs. Pp. 131–142 in: *Teaching Clay Science, CMS Workshop Lectures*, **11** (A. Rule and S. Guggenheim, editors). The Clay Minerals Society, Aurora, Colorado, USA.

Eberl, D.D. and Środoń, J. (1988) Ostwald ripening and interparticle-diffraction effects for illite crystals. *American Mineralogist*, **73**, 1335–1345.

Eberl, D.D., Środoń, J., Lee, M., Nadeau, P., and Northrop, R.H. (1987) Sericite from the Silverton caldera: Correlation among structure, composition, origin and particle thickness. *American Mineralogist*, **72**, 914–935.

Eberl, D.D., Środoń, J., Kralik, M., Taylor, B.E., and Peterman, Z.E. (1990) Ostwald Ripening of clays and metamorphic minerals. *Science*, **248**, 474–477.

Eberl, D.D., Drits, V., Środoń, J., and Nüesch, R. (1996) MudMaster: A program for calculating crystallite size distributions and strain from the shapes of X-ray diffraction peaks. *U.S. Geological Survey Open-File Report 96-171*, 46 pp.

Eberl, D.D., Drits, V.A., and Środoń, J. (1998a) Deducing crystal growth mechanisms for minerals from the shapes of crystal size distributions. *American Journal of Science*, **298**, 499–533.

Eberl, D.D., Nüesch, R., Šucha, V., and Tsipursky, S. (1998b) Measurement of fundamental illite particle thicknesses by X-ray diffraction using PVP-10 intercalation. *Clays and Clay Minerals*, **46**, 89–97.

Eberl, D.D., Drits, V.A., and Środoń, J. (2000) User's guide to GALOPER – a program for simulating the shapes of crystal size distributions and associated programs. *U.S. Geological Survey Open File Report*, OF00-505, 44 pp.

Eberl, D.D., Środoń, J., and Drits, V.A. (2003) Comment on "Evaluation of X-ray diffraction methods for determining the crystal growth mechanisms of clay minerals in mudstones, shales and slates," by L.N. Warr and D.L. Peacor, *Schweizerische Mineralogische Petrographische Mitteilungen*, **83**, 349–358.

Frank, F.C. (1949) The influence of dislocations on crystal growth: Discussions. *Faraday Society*, **5**, 48.

Hedenquist, J.W. and Lowenstern J.B. (1994) The role of magmas in the formation of hydrothermal ore deposits. *Nature*, **370**, 519–527.

Higashi, S. (1982) Tobelite, a new ammonium dioctahedral mica. *Mineralogical Journal*, **11**, 138–146.

Inoue, A. and Kitagawa, R. (1994) Morphological characteristics of illitic clay minerals from a hydrothermal system. *American Mineralogist*, **79**, 700 –711.

Inoue, A., Utada, M. and Wakita, K. (1992) Smectite-to-illite conversion in natural hydrothermal systems. *Applied Clay Science*, **7**, 131–145.

Inoue, A., Velde, B., Meunier, A., and Touchard, G. (1988) Mechanism of illite formation during smectite-to-illite conversion in a hydrothermal system. *American Mineralogist*, **73**, 241–249.

Jackson, M.L. (1975) *Soil Chemical Analysis – Advanced Course.* Published by the author, Madison, Wisconsin, USA, 895 pp.

Kitagawa, R. (1992) Surface microtopographies of pyrophyllite from the Shokozan area, Chugoku Province, southwest Japan. *Clay Science*, **8**, 285–295.

Kitagawa, R. (1995) Coarsening process of a hydrothermal sericite sample using surface microtopography and transmission electron microscopy techniques. Pp. 249–252 in: *Clays Controlling the Environment* (J. Churchman, R.W. Fitzpatrick, and R.A. Eggleton, editors). Proceedings of the International Clay Conference, Adelaide, Australia.

Kitagawa, R. and Matsuda, T. (1992) Microtopography of regularly-interstratified mica and smectite. *Clays and Clay Minerals*, **40**, 114–121.

Komatsu, H. and Sunagawa, I. (1965) Surface structures of sphalerite crystals. *American Mineralogist*, **50**, 1046–1057.

Kotarba, M. and Środoń, J. (2000) Diagenetic evolution of crystallite thickness distribution of illitic material in Carpathian shales, studied by the Bertaut-Warren-Averbach XRD method (MudMaster computer program). *Clay Minerals*, **35**, 383–391.

Krumbein, W.C. and Graybill, F.A. (1965) *An Introduction to Statistical Models in Geology*. McGraw Hill Company, New York, 475 pp.

Masterton, W.L., Slowinski, E.J., and Stanitski, C.L. (1981) *Chemical Principles*. Holt-Saunders International Edition, Philadelphia, Pennsylvania, USA, 641 pp.

McHardy, W.J. and Birnie, A.C. (1987) Scanning electron microscopy. Pp. 74–208 in: *A Handbook of Determinative Methods in Clay Mineralogy* (M.J. Wilson, editor). Blackie, Glasgow, UK.

Meyer, C. and Hemley, J.J. (1967) Wall-rock alteration. Pp. 166–235 in: *Geochemistry of Hydrothermal Ore Deposits* (H.L. Barnes, editor). Holt, Rinehart, and Winston, New York.

Moore, D.M. and Reynolds, R.C. (1997) *X-ray diffraction and the Identification and Analysis of Clay Minerals.* Oxford University Press, New York, 381 pp.

Mystkowski, K., Środoń, J., and Elsass, F. (2000) Mean thickness and thickness distribution of smectite crystallites. *Clay Minerals*, **35**, 545–557.

Nadeau, P.H., Wilson, M.J., McHardy, W.J., and Tait, J.M. (1985) The conversion of smectite to illite during diagenesis. Evidence from some illitic clays from bentonites and sandstones. *Mineralogical Magazine*, **49**, 393–400.

Peltz, S., Vâjdea, E., Balogh, K., and Pécskay, Z. (1987) Contributions to the chronological study of the volcanic processes in the Cãlimani and Harghita Mountains (East Carpathians, Romania). *Compte Rendu de Institute de Geologie e Geofisique*, **72-73/1**, 323–338, Bucharest.

Rãdulescu, D.P. and Sãndulescu, M. (1973) The plate-tectonics concept and the geological structure of the Carpathians. *Tectonophysics*, **16**, 155–161.

https://doi.org/10.1346/CCMN.2013.0610415 Published online by Cambridge University Press

Rădulescu, D.P., Peltz, S., and Stanciu, C. (1973) Neogene volcanism in the East Carpathians (Călimani-Gurghiu-Harghita Mts.). *Guide to Excursion 2AB. Symposium: Volcanism and Metallogenesis*, Bucharest.

Reynolds, R.C. (1985) *NEWMOD, a computer program for the calculation of one dimensional diffraction patterns of mixed layered clays*. Published by the author, Hanover, New Hampshire.

Royden, L.H. (1988) Late Cenozoic tectonics of the Pannonian Basin System. *American Association Petroleum Geology Memoir*, **45**, 27–28.

Săndulescu, M. (1984) *Geotectonics of Romania.* Technical Publishing House, Bucharest, 336 pp (in Romanian).

Seghedi, I., Balintoni, I., and Szakacs, A. (1998) Interplay of tectonics and Neogene post-collisional magmatism in the intracarpathian area. *Lithos*, **45**, 483–499.

Seghedi, I., Downes, H., Szakacs, A., Mason, P.R.D., Thirlwall, M.F., Rosu, E., Pécskay, Z., Márton, E., and Panaiotu, C. (2004) Neogene-Quaternary magmatism and geodynamics in the Carpathian–Pannonian region: a synthesis. *Lithos*, **72**, 117–146.

Sillitoe, R.H. (2010) Porphyry copper systems. *Economic Geology*, **105**, 3–41.

Środoń, J., Eberl, D.D., and Drits, V. (2000) Evolution of fundamental particle size during illitization of smectite and implications for reaction mechanism. *Clays and Clay Minerals*, **48**, 446–458.

Stanciu, C. (1984) Hypogene alteration of Neogene volcanism of the East Carpathians. *Annuare de Institute de Geologique e Geofisique*, **LXIV**, 182–193, Bucharest.

Sunagawa, I. (1960) Mechanism of crystal growth, etching, and twin formation of hematite. *Mineralogical Journal*, **3**, 59–89.

Sunagawa, I. (1961) Step height of spirals on natural hematite crystals. *American Mineralogist*, **46**, 1216–1226.

Sunagawa, I. (1962) Mechanism of growth of hematite. *American Mineralogist*, **47**, 1139–1155.

Sunagawa, I. (1964) Growth spirals on phlogopite crystals. *American Mineralogist*, **49**, 1427–1434.

Sunagawa, I. and Koshino (1975) Growth spirals on kaolin group minerals. *American Mineralogist*, **60**, 401–412.

Szakacs, A. and Seghedi, I. (1995) The Călimani-Gurghiu-Harghita volcanic chain, Eastern Carpathians, Romania: volcanological features. *Acta Vulcanologica*, **7**, 145–153.

Verma, A.R. (1956) A phase contrast microscopic study of the surface structure of blende crystals. *Mineralogical Magazine*, **31**, 136.

Warr, N.L. and Nieto, F. (1998) Crystallite thickness and defect density of phyllosilicates in low-temperature metamorphic pelites: a TEM and XRD study of clay-mineral crystallinity index standards. *The Canadian Mineralogist*, **36**, 1453–1474.

Williams, L.B. and Hervig, R.L. (2006) Crystal size dependence of illite-smectite isotope equilibration with changing fluids. *Clays and Clay Minerals*, **54**, 531–540.

(*Received 7 October 12; revised 23 July 13; Ms. 717; AE: W. Huff*)

https://doi.org/10.1346/CCMN.2013.0610415 Published online by Cambridge University Press